nature communications

Article

https://doi.org/10.1038/s41467-024-55620-0

The degradation mechanism of multi-resonance thermally activated delayed fluorescence materials

Received: 17 April 2024

Accepted: 18 December 2024

Published online: 04 January 2025

Check for updates

Byung Hak Jhun[1,6], Yerin Park[2,3,6], Hwang Suk Kim[4,6], Ji Hye Baek[1], Joonghyuk Kim[4], Eunji Lee[2,3], Hyejin Moon[2,3], Changjin Oh[2,3], Yongsik Jung[4] ✉, Seunghee Choi[5], Mu-Hyun Baik[2,3] ✉ & Youngmin You[1] ✉

1,4-Azaborine-based arenes are promising electroluminescent emitters with thermally activated delayed fluorescence (TADF), offering narrow emission spectra and high quantum yields due to a multi-resonance (MR) effect. However, their practical application is constrained by their limited operational stability. This study investigates the degradation mechanism of MR-TADF molecules. Electroluminescent devices incorporating these compounds display varied operational lifetimes, uncorrelated with excitonic stability or external quantum efficiency roll-off. Bulk electrolysis reveals significant instability in the radical cationic forms of MR-TADF compounds, with device lifetime linked to the Faradaic yield of oxidation. Comprehensive chemical analyses corroborate that the degradation byproducts originated from intramolecular cyclization of radical cation, followed by hydrogen atom transfer. The mechanism is further supported by enhanced stability observed in a deuterated MR-TADF emitter, attributed to a secondary kinetic isotope effect. These findings provide insights into the stabilizing effects of deuteration and mechanism-driven strategies for designing MR-TADF compounds with improved operational longevity.

Organic light-emitting devices (OLEDs) have undergone significant advancements over the past two decades, with notable improvements in efficiency and color purity. These advances are largely due to the discovery of novel emitters, including luminescent molecules capable of exciton harvesting. Among these, cyclometalated complexes of Ir(III)[1–5] and Pt(II)[6,7], as well as organic[8,9] and organometallic compounds[10] that exhibit thermally activated delayed fluorescence (TADF), stand out. The multi-resonance (MR)-TADF emitters, in particular, have attracted considerable attention. For instance, aromatic 1,4-azaborine scaffolds housing complementary boron and nitrogen atoms produce exceptionally narrow fluorescence spectra, accompanied by photoluminescence quantum yields approaching unity[11–13]. The unique emission behavior positions MR-TADF compounds as promising candidates for meeting the demanding requirements of commercial OLED applications[14–19].

Despite their potential, the widespread adoption of MR-TADF molecules is hampered by their instability under the operational conditions in the device. This issue is not unique to MR-TADF molecules. It mirrors challenges faced by earlier generations of phosphorescent[20–28] and dipolar TADF emitters[29–32], which also degrade through mechanisms that produce exciton quenchers, charge carrier traps, and non-emissive charge carrier recombination centers, adversely affecting OLED performance[33,34].

[1]Department of Chemical and Biomolecular Engineering, Yonsei University, Seoul 03722, Republic of Korea. [2]Department of Chemistry, Korea Advanced Institute of Science and Technology (KAIST), Daejeon 34141, Republic of Korea. [3]Center for Catalytic Hydrocarbon Functionalizations, Institute for Basic Science (IBS), Daejeon 34141, Republic of Korea. [4]Samsung Advanced Institute of Technology, Samsung Electronics Co. Ltd, Suwon-si, Gyeonggi-do 16678, Republic of Korea. [5]Division of Chemical Engineering and Materials Science, Ewha Womans University, Seoul 03760, Republic of Korea. [6]These authors contributed equally: Byung Hak Jhun, Yerin Park, Hwang Suk Kim. ✉e-mail: ys327.jung@samsung.com; mbaik2805@kaist.ac.kr; odds2@yonsei.ac.kr

Consequently, a deeper understanding of the degradation mechanisms of MR-TADF materials is crucial for enhancing their operational longevity. Notably, Lee et al. discovered that TADF-inactive MR fluorescent emitters could achieve longer operational lifetimes than their TADF-active counterparts[35], a finding echoed by Meng et al.[36], who attributed this to the intrinsic instability of long-lived triplet excitons in MR-TADF emitters. In-situ Raman spectroscopy studies suggested that MR-TADF excitons contribute to the morphological instability of emitting layers[37]. Furthermore, Wang et al. have shown that incorporating an additional boracycle into MR-TADF emitters can extend operational lifetimes, a benefit theorized to stem from increased anionic stability, as supported by quantum chemical calculations[38]. While these studies have proposed various factors contributing to reduced operational lifetimes, direct chemical evidence identifying the specific intermediates and pathways of degradation remains scarce. Given that an OLED's operational lifetime is primarily determined by the intrinsic stability of its components[24], elucidating the degradation process of MR-TADF molecules is of paramount importance.

In this study, we delve into the intricate chemical mechanisms underlying the intrinsic degradation of a series of blue-emissive MR-TADF molecules, as illustrated in Fig. 1. Through comprehensive chemical analyses, we obtained direct experimental evidence indicating that the primary degradation pathway of MR-TADF materials is initiated by hole trapping. Both experimental observations and quantum chemical simulations suggest that the degradation process involves a dehydrogenative cyclization reaction of the radical cationic species. This mechanism elucidates the observed enhanced operational stability of a deuterated MR-TADF emitter compared to its undeuterated counterpart, attributing it to the secondary kinetic isotope effect on the rate-determining cyclization step in the deuterated molecule (*vide infra*).

Results

Operational stabilities of MR-TADF OLEDs

For this investigation, we selected 5,9-bis(4-biphenyl)-2,12-diphenyl-5,9-diaza-13b-boranaphtho[3,2,1-*de*]anthracene (**1**), N^7,N^7,N^{13},N^{13},5,9,11,15-octaphenyl-5,9,11,15-tetrahydro-5,9,11,15-tetraaza-19b,20b-diboradinaphtho[3,2,1-*de*:1′,2′,3′-*jk*]pentacene-7,13-diamine (*ν*-DABNA[12] and denoted as **2** in this study), 5,9-bis(4-biphenyl)-7-*N*-(2-biphenyl)-*N*-(4-biphenyl)amino-2,12-diphenyl-5,9-diaza-13b-boranaphtho[3,2,1-*de*] anthracene (**3**), and 5,9-bis(4-*tert*-butylphenyl)-2,12-di(*tert*-butyl)-5,9-diaza-13b-boranaphtho[3,2,1-*de*]anthracene (*t*-DABNA[39] and denoted as **4** in this study) shown in Fig. 1. The photophysical characteristics of these compounds were assessed using thin films of poly(methyl methacrylate) (PMMA) doped with 2 wt% of the MR-TADF compounds, and the results are summarized in Table 1. Compounds **1**–**4** displayed pronounced blue fluorescence, with emission peak wavelengths ranging from 459 to 471 nm, full widths at half-maximum (FWHM) values between 775 and 1130 cm^{-1}, and photoluminescence quantum yields (Φ_{PL}) from 0.96 to 1.00. The delayed fluorescence lifetimes (τ_{DF}s) of these compounds span from 3.8 to 111 µs, indicative of moderate energy differences between the singlet and triplet excited states (ΔE_{ST}, 0.11–0.27 eV). These photophysical parameters collectively underscore the MR-TADF properties of compounds **1**–**4**.

The electroluminescence performances of compounds **1**–**4**, utilized as dopants, were assessed using a specific device configuration, comprising an indium tin oxide (ITO) anode, a hole-injection layer of *p*-doped (3 wt% NDP series, Novaled AG) *N*-([1,12-biphenyl]-4-yl)-9,9-dimethyl-*N*-(4-(9-phenyl-9*H*-carbazol-3-yl)phenyl)-9*H*-fluoren-2-amine (BCFA) (10 nm), a hole-transporting layer of BCFA (135 nm), an electron-blocking layer of 2,2′-di(9*H*-carbazole-9-yl)-1,1′-biphenyl (oCBP) (5 nm), an exciton-blocking layer of 3′,5′-di-9*H*-carbazol-9-yl-[1,1′-biphenyl]-2-carbonitrile (mCPD) (5 nm), an emission layer (40 nm), a hole-blocking layer of 9-(3-(9*H*-carbazol-9-yl)phenyl)-9*H*-carbazole-3,6-dicarbonitrile (mCP-2CN) (10 nm), an electron-transporting layer co-deposited with dibenzo[*b*,*d*]furan-2,8-diylbis(diphenylphosphine oxide) (DBFPO) and lithium 8-hydroxyquinolinate (LiQ) (30 nm), an electron-injecting layer of LiQ (9 nm), and an aluminum (Al) cathode (100 nm). The emission layer, comprising a 1.5 wt% dopant, utilized a ternary composition, including a 9-(3-biphenyl)-3,9′-bicarbazole hole-transporting (HT) host, a 3′-(9-(3-cyanocarbazolyl))-5′-cyano-3-(9-carbazolyl)biphenyl electron-transporting (ET) host, in a volumetric ratio of 6:4. The chemical structures and energy levels of the constituent materials are displayed in Fig. 2a. Electroluminescence spectra, recorded at an intensity of 1000 cd m^{-2}, revealed peak wavelengths of 474 nm for compounds **1** and **2**, 465 nm for compound **3**, and 462 nm for compound **4**, as shown in Fig. 2b. The FWHM values as small as 890–1300 cm^{-1} and the Commission internationale de l'éclairage coordinate *y* values (CIE_y) approaching 0.10 demonstrate the validity of the MR-TADF molecules as blue emitters.

The devices incorporating **1**–**4** demonstrate negligible differences in their current density profiles, as depicted in Fig. 2c. This uniformity can be attributed to the similar energy offsets between the highest occupied molecular orbitals (HOMOs) of **1**–**4** and the HT host ranging from 0.4 to 0.5 eV. The maximum external quantum efficiency (EQE_{max}) across these devices is identified to lie between 22.5% and 26.7% (Table 2). Figure 2d reveals that devices based on compounds **1**, **3**, and **4** experience moderate EQE roll-off, whereas the device utilizing compound **2** shows a relatively suppressed roll-off due to the

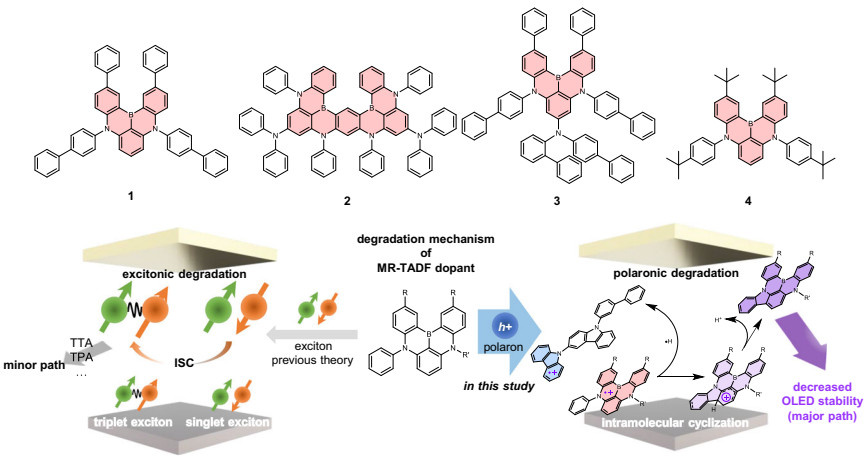

Fig. 1 | Oxidative degradation of MR-TADF dopants. Chemical structures of the MR-TADF dopants and a schematic of the degradation mechanism of an MR-TADF dopant, as established in the present study.

https://doi.org/10.1038/s41467-024-55620-0

Table 1 | Photophysical and electrochemical data, and yields for intrinsic degradation of the MR-TADF dopants

	λ_{em} (nm)[a,b]	Φ_{PL} (%)[a,c]	τ_{PF} (ns)[a,d]	τ_{DF} (μs)[a,e]	k_r^{TADF} (10^4 s^{-1})[f]	k_{rISC} (10^5 s^{-1})[g]	E_{T1} (eV)[a,h]	ΔE_{ST} (eV)[a,i]	E_{ox} (V vs SCE)[j]	Φ_{deg} (%)[k]	Faradaic yield (%)[l]
1	471	96	11	78	5.1	1.8	2.49	0.27	0.98	0.29	37
2	467	98	6	3.8	6.3	6.2	2.64	0.11	0.92	0.92	46
3	461	98	7	28	5.6	4.1	2.57	0.21	0.97	0.68	59
4	459	100	5	111	5.4	1.1	2.54	0.25	0.90	0.22	79
1D	473	94	10	62	5.5	1.5	2.49	0.24	0.95	0.18	30

[a]2 wt% in PMMA films, 300 K. See Supplementary Fig. 1 for the UV–Vis absorption and photoluminescence spectra recorded in tetrahydrofuran (THF).
[b]Emission peak wavelength. See Supplementary Fig. 2 for the photoluminescence spectra of the PMMA films.
[c]Photoluminescence quantum yield determined absolutely using an integrating sphere.
[d]Lifetime of prompt fluorescence.
[e]Lifetime of delayed fluorescence.
[f]Radiative rate constant, $k_r^{TADF} = \Phi_{PL}/\tau_{obs}$, where τ_{obs} is the average fluorescence lifetime.
[g]Rate constant for reverse intersystem crossing, $k_{rISC} = (\Phi_{total} \times k_{PF} \times k_{DF})/k_r^{S1}$.
[h]Energy of the triplet state.
[i]The energy difference between the singlet and the triplet excited states. Refer to Supplementary Fig. 3 for details.
[j]Oxidation potential determined by cyclic voltammetry (CV) and differential pulse voltammetry (DPV) for Ar-saturated THF containing 1.0 mM dopant and 0.10 M tetrabutylammonium hexafluorophosphate; A glassy carbon disk and a Pt wire for the working and counter electrodes, respectively; an $Ag/AgNO_3$ pseudo-reference electrode; scan rates = 0.1 V s^{-1} (CV) and 4 mV s^{-1} (DPV). See Supplementary Fig. 4 for the voltammograms.
[k]Quantum yield for photolysis.
[l]Faradaic yield for oxidative bulk electrolysis.

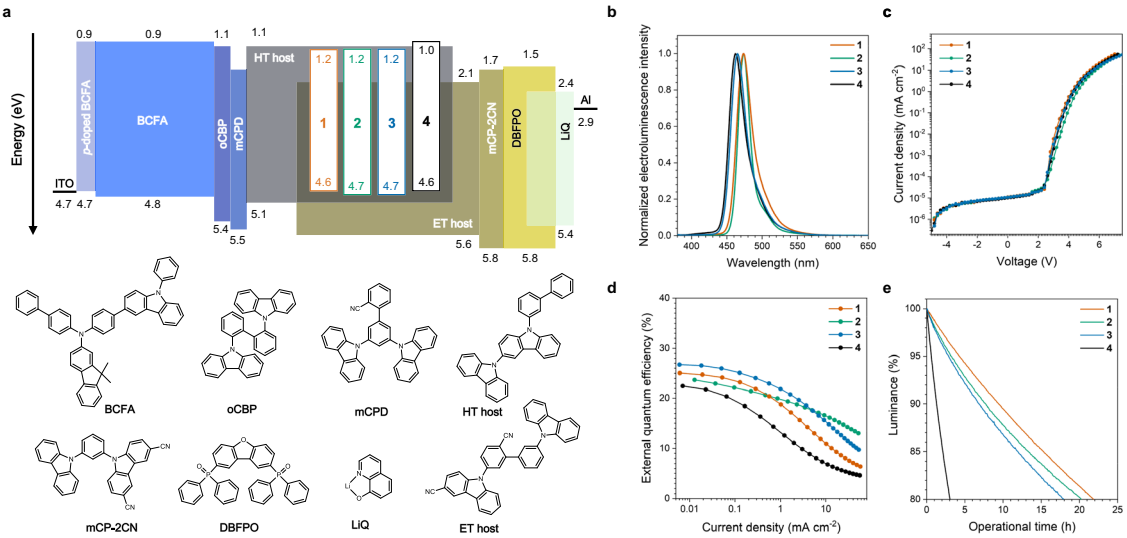

Fig. 2 | Electroluminescence performance. a Schematic of the configuration of the electroluminescence devices tested, including the energy levels and chemical structures of their component materials. **b** Electroluminescence spectra. **c** Current density–voltage curves. **d** External quantum efficiencies as a function of current density. **e** Percent luminance decays as a function of operation time driven at a constant current density at an initial luminance of 1000 cd m^{-2}.

Table 2 | Device performance

	V (V)[a]	J (mA cm^{-2})[a]	CIE (x, y)[a]	EQE (%)	Power efficiency (lm W^{-1})	LT_{95} (h)
1	5.14	7.00	(0.11, 0.17)	25.1[b]/12.3[a]	30.9[b]/8.79[a]	4.3[c]/5.4[d]
2	5.38	5.75	(0.11, 0.15)	23.7[b]/17.4[a]	21.3[b]/10.2[a]	3.2[c]/3.3[d]
3	5.25	6.53	(0.13, 0.11)	26.7[b]/16.8[a]	24.5[b]/9.19[a]	2.9[c]/3.3[d]
4	6.11	20.0	(0.13, 0.10)	22.5[b]/5.8[a]	20.0[b]/2.57[a]	0.60[c]/2.6[d]

[a]Values at a luminance of 1000 cd m^{-2}.
[b]Maximum values.
[c]Operation time when the luminance decreases to 95% of its initial value at an initial luminance of 1000 cd m^{-2}.
[d]Operation time when the luminance decreases to 95% of its initial value of device-driven under a constant current density of 5 mA cm^{-2}. See Supplementary Fig. 5 for plots of the luminance and power efficiency as functions of current density.

significantly shorter delayed fluorescence lifetime (τ_{DF}) of 3.8 μs, compared to 28–111 μs for the other MR-TADF compounds. These varying roll-off profiles hint at the presence of triplet–triplet annihilation or triplet–polaron annihilation processes, which are recognized as major degradation pathways for high-energy blue emitters, generating unstable species that significantly shorten device operational lifetimes[20,24,40]. Nonetheless, there appears to be no direct correlation between the operational stability and EQE roll-off behaviors (Fig. 2e). For instance, devices **1** and **3**, despite showing substantial EQE roll-off, exhibit LT_{95} (the time at which luminance decreases to 95% of

its initial value at 1000 cd m^{-2}) values of 4.3 and 2.9 h, respectively, comparable to the 3.2 h of device **2** that has the least EQE roll-off. Moreover, device **4**, despite having an EQE roll-off profile similar to that of devices **1** and **3**, presents the shortest LT_{95} value of only 0.6 h. This observation suggests that the lifetime of these devices may not be predominantly determined by the bimolecular annihilation processes involving excitons.

Degradation intermediates

To elucidate the degradation mechanisms, we conducted both photolysis and bulk electrolysis experiments for deaerated solutions of the MR-TADF dopants. These experiments aimed to simulate the excitonic and polaronic degradation pathways, respectively, facilitating the identification of crucial degradation intermediates. Note that although solution experiments do not perfectly replicate the degradation processes in emitting layers within the device, we chose this approach because it offers several advantages, including controlled charge-carrier injection and high yields for the degradation byproduct formation. Photolysis was performed in argon-saturated tetrahydrofuran (THF) solutions containing 100 μM of compounds **1**–**4**, under continuous illumination with monochromatic light of 450 nm wavelength (photon flux = 4.0×10^8 Einstein s^{-1}). The progression of photolytic degradation was monitored using high-performance liquid chromatography (HPLC) due to the inadequacy of UV–Vis absorption spectroscopy for quantitative analysis. The quantum yield for degradation (Φ_{deg}) was determined to be under 1% (Table 1 and Fig. 3c), and importantly, Φ_{deg} exhibited no significant correlation with LT_{95}, suggesting that excitonic degradation does not primarily influence the operational stability (for additional details and discussion, see Supplementary Figs. 6 and 7). It is important to note that k_{rISC} shows no correlation with either the quantum yield of photolysis or LT_{95} (Table 1). This further suggests that excitonic degradation has a negligible impact on operational stability.

In marked contrast, radical cation forms of the MR-TADF molecules demonstrated pronounced instability during oxidative bulk electrolysis at anodic potentials, as quantified by HPLC (detailed in Fig. 3a, b, and their captions). Reductive bulk electrolysis was not considered, given the electron-scattering nature of the MR-TADF molecules, as inferred from the positions of their lowest unoccupied molecular orbitals (LUMOs) illustrated in Fig. 2a. By contrast, the MR-TADF compounds can trap hole carriers from the HT host with driving forces of 0.4–0.5 eV. The Faradaic yields for oxidative bulk electrolysis, representing the ratio of decomposed compound quantity to the electrons transferred, were significantly higher by two orders of magnitude compared to Φ_{deg} (as shown in Table 1 and Fig. 3c). Although these solution-based experiments do not perfectly mimic the polaronic degradation in the emissive layers, they underscore the notably lesser stability of the MR-TADF compounds' radical cations compared to their excitons. Moreover, an inverse correlation was observed between LT_{95} and the Faradaic yield (see Fig. 3d). While not definitive, this negative linear relationship implies a close association between the positive polarons of MR-TADF molecules and the operational stability of OLEDs.

The observed relationship between the operational stability of OLEDs and the stability of MR-TADF molecules is further supported by examining the behavior of trapped hole carriers within these dopants. The ideality factor $[(k_BT/q)\cdot(\partial \ln J/\partial V)]^{-1}$ for devices using compounds **1**–**4** consistently exceeds two, as shown in Supplementary Fig. 9, where k_B is the Boltzmann constant, T is the absolute temperature, q is the elementary charge, J is the current density, and V is the voltage. This finding suggests significant charge carrier trapping within the MR-TADF molecules[41]. In single carrier devices designed for exclusive hole transport, the hole current density profiles vary according to the specific MR-TADF dopant used, as depicted in Supplementary Fig. 10. In contrast, no significant variation in current density is observed with exclusive electron transport (Supplementary Fig. 11). The sequence of hole trapping within the dopants is observed to follow the order **2** > **4** ~ **3** > **1**. This order, in conjunction with the Faradaic yield data, offers a coherent kinetic rationale for the observed LT_{95} values of the OLED devices. This rationale is predicated on the assumption that the degradation rate adheres to pseudo-first-order kinetics, with the rate equation modeled as rate = $k\cdot[\mathbf{D}^{\bullet+}] = \exp(-E_a/k_BT)\cdot[\mathbf{D}^{\bullet+}]$, where k is the rate constant for degradation, $[\mathbf{D}^{\bullet+}]$ is the molar concentration of the radical cation of an MR-TADF dopant, and E_a is the activation energy for the rate-determining step. Under this framework, the device utilizing compound **1** exhibits the longest LT_{95}, attributable to molecule **1** having the smallest Faradaic yield, indicative of the highest intrinsic stability, and the lowest density of positive polarons, leading to the lowest concentration of the degradation intermediates. Conversely, the notably shorterLT_{95} for the device incorporating compound **4** can be explained by its high Faradaic yield and dense population of positive polarons, highlighting a direct correlation between these factors and device longevity.

Degradation mechanism

To shed light on the degradation mechanism of MR-TADF materials, we analyzed a byproduct formed from radical cations. Electrospray ionization (ESI) mass spectrometry in positive mode revealed a significant peak at an m/z value of 810.51 amu in an electrolyzed solution of compound **4**, as shown in Fig. 4a. This peak corresponds to a species involving [**4**−2H], precisely matching with the theoretical isotope distribution. Notably, the pristine sample of **4** lacks this peak, underscoring that the cyclization product specifically arises from the radical cation state. This structural assignment gains additional support from the appearance of new peaks in the ^{1}H NMR (300 MHz, CD_2Cl_2) spectrum, indicative of a non-symmetric aromatic framework formation, as depicted in Fig. 4b. An independently synthesized non-symmetric cyclization compound (labeled as compound **4′**, see Fig. 4b) shows ^{1}H NMR peaks corresponding to those observed in the oxidation byproduct. We also found the formation of mono-, bi-, tri-, and tetra-cyclization byproducts of **2** with multiple reaction sites (Supplementary Fig. 12), which corroborates the occurrence of oxidative cyclization reactions. Note that this observation aligns with the known intramolecular electrochemical reactivities of aryl amines: aryl amines cyclize upon oxidation which typically involves radicals formed at the *ortho*-position to the amino group[42,43]. Aryl amines are also known to undergo oxidation and subsequent electrochemical polymerization under electrical stress, adversely affecting the device's lifetime. Protective groups like *tert*-butyl substituents or oxidation-stable replacements are commonly used to enhance their electrochemical stability and improve device performance[44–47].

Further evidence for the intermediacy of the radical cation in the cyclization reaction comes from spectroelectrochemical measurements. Upon applying an anodic potential of 1.04 V versus a saturated calomel electrode (SCE) to an argon-saturated THF solution containing 10 μM of compound **4** and 0.10 M tetrabutylammonium hexafluorophosphate as supporting electrolyte, a broad absorption band appears in the 500–700 nm region (Fig. 4c). This absorption signature is replicated upon the electrochemical oxidation of **4** with [$FeCl_3$] as a strong oxidant (Fig. 4d), signifying that the visible absorption band originates from the radical cation of a cyclized compound. This is corroborated by the identical absorption band observed upon the electrochemical oxidation of compound **4′** at a potential of 0.80 V vs SCE (Fig. 4e). Collectively, our experimental findings converge on the oxidative cyclization as a pivotal degradation pathway of the MR-TADF molecule.

We performed a mechanistic investigation using DFT calculations to propose the major degradative mechanism and the key kinetic factor governing the stability of MR-TADF dopants against oxidative degradation. Our initial analysis of bond dissociation energies showed

https://doi.org/10.1038/s41467-024-55620-0

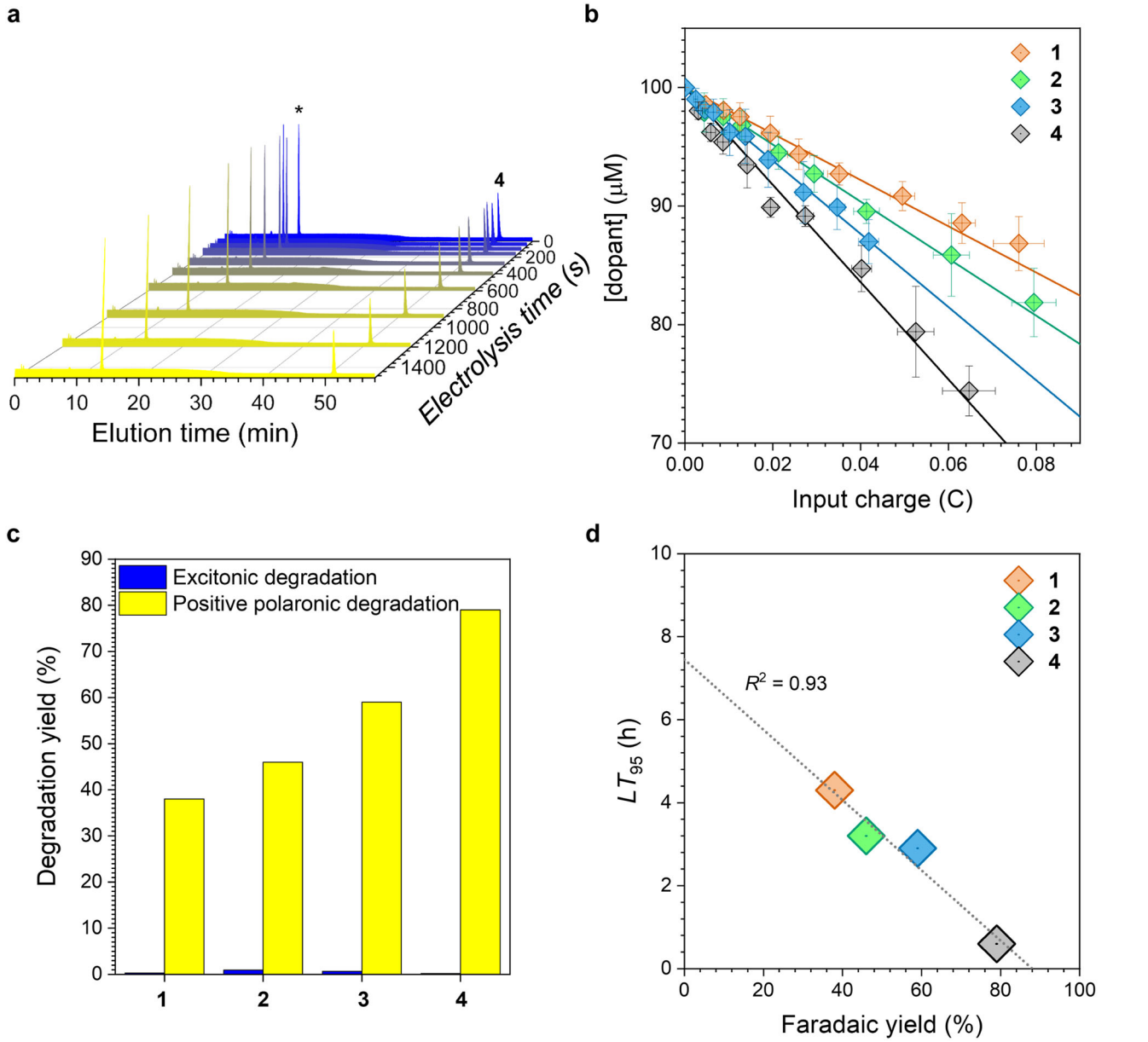

Fig. 3 | Oxidative degradation. a Liquid chromatograms of 100 μM **4** (Ar-saturated THF containing a 0.10 M tetrabutylammonium hexafluorophosphate supporting electrolyte) obtained during oxidative bulk electrolysis performed at an anodic potential of 1.04 V vs SCE. A Pt mesh and a Pt coil were used for the working and the counter electrodes, respectively. An $Ag/AgNO_3$ pseudo-reference electrode was used. The peak marked with an asterisk (*) corresponds to a benzophenone internal standard. Chromatograms for **1**–**3** are shown in the Supplementary Fig. 8. **b** Decay in the concentration of the residual MR-TADF dopants during continuous oxidative bulk electrolysis performed at potentials of 1.04 V vs SCE (**1** and **4**), 1.01 V vs SCE (**2**), and 0.98 V vs SCE (**3**). Error bars represent the standard deviation of three independent experiments. The solid lines are linear fits of the initial five data points. **c** Quantum yields for photolysis (blue bars) and Faradaic yields for oxidative electrolysis (yellow bars) of **1**–**4**. Values are compiled in Table 1. **d** Correlation between LT_{95} and the Faradaic yield for the oxidative degradation of the dopants. The gray line is a linear fit.

that the C–C single bonds in the dopant molecule become stronger upon oxidation (see Supplementary Table 1). This unexpected increase in bond strength is attributed to an increase in bond order after removing one electron from the HOMO, which has an antibonding character between the aromatic rings. As a result, unimolecular degradation is unlikely to be the primary degradation route.

Further investigation into bimolecular reactions evaluated various mechanistic scenarios, as outlined in Fig. 5. To assess the general reactivity of a series of dopants, we used a simplified model structure without peripheral substituents (denoted as **M**) and a truncated host molecule (denoted as **Host**) as the reaction partner. Two potential reaction modes for the oxidized dopant (denoted as $\mathbf{M}^{\bullet+}$) were considered: acting as a radical or as a cation. $\mathbf{M}^{\bullet+}$ could undergo deprotonation by **Host** due to increased acidity upon oxidation (path a) or engage in hydrogen atom transfer to dissipate spin density (path b). In both scenarios, the C–H bond cleavage was accompanied by the formation of a new C–C bond, resulting in cyclization. When cyclization did not accompany C–H bond activation, highly unstable open-shell species were generated, making the process energetically unfavorable (see Supplementary Fig. 13).

We then modeled the oxidized host ($\mathbf{Host}^{\bullet+}$) as the reaction partner, reflecting the presence of hole-transporting hosts in the device environment. For hydrogen atom abstraction by $\mathbf{Host}^{\bullet+}$ (path c), our kinetic analysis showed a substantial reduction in the reaction

https://doi.org/10.1038/s41467-024-55620-0

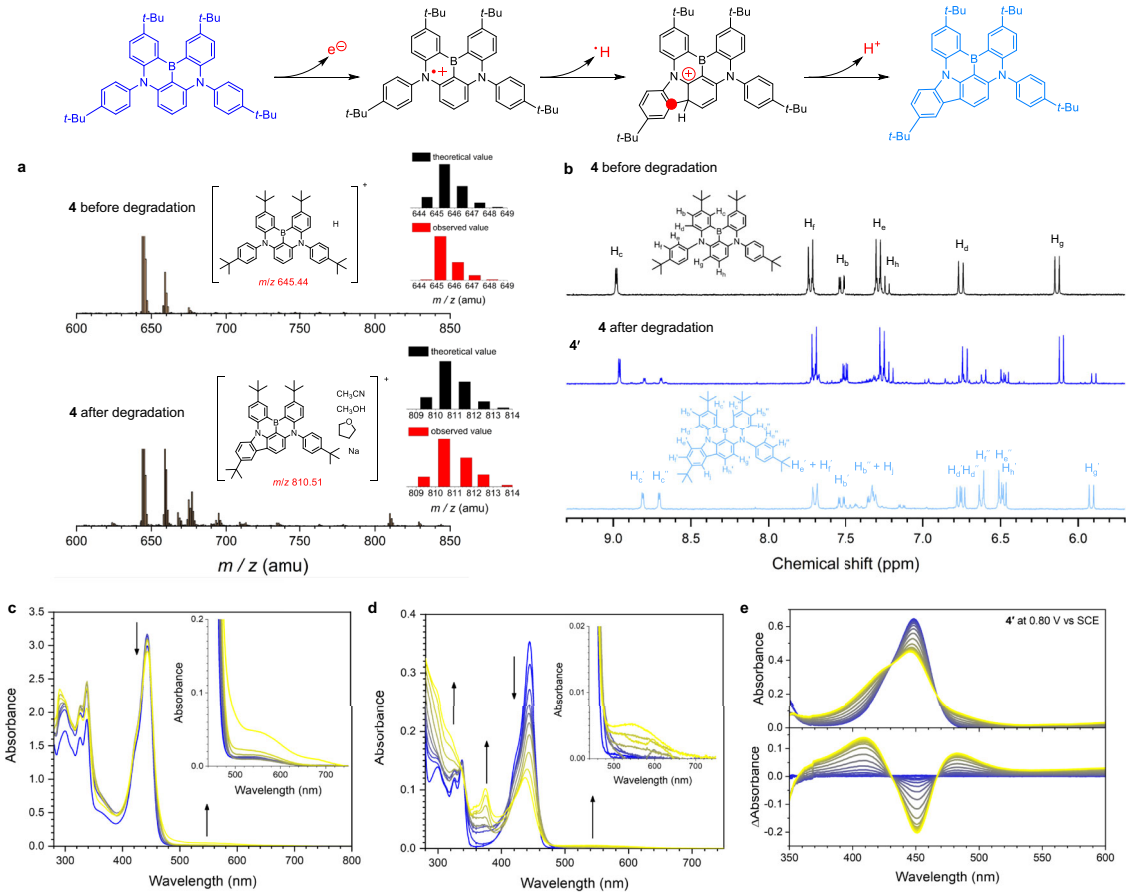

Fig. 4 | Degradation byproduct. a Mass spectra (ESI, positive) of 100 μM **4** (Ar-saturated THF containing a 0.10 M tetrabutylammonium hexafluorophosphate supporting electrolyte) obtained before (top panel) and after (bottom panel) oxidative bulk electrolysis at an anodic potential of 1.04 V vs SCE. A Pt mesh and a Pt coil were used for the working and the counter electrodes, respectively. An Ag/$AgNO_3$ pseudo reference electrode was used. The inset structures are the proposed chemical structures corresponding to the indicated *m/z* values. The inset black and red bars show the theoretical and observed *m/z* values, respectively. **b** ^{1}H NMR (300 MHz, CD_2Cl_2) spectra of **4** before (top) and after (middle) the oxidative degradation, and the independently synthesized cyclization byproduct **4′** (bottom). **c** UV–Vis absorption spectra of 10 μM **4** (Ar-saturated THF containing 0.10 M tetrabutylammonium hexafluorophosphate) obtained during oxidative electrolysis (0–3 h) at an anodic potential of 1.04 V vs SCE. Arrows indicate spectral changes. The inset figure depicts the magnified view in the region 440–750 nm. **d** UV–Vis absorption spectra of 100 μM **4** reacted with 1 equiv [$FeCl_3$] (Ar-saturated CH_2Cl_2). Arrows indicate spectral changes. The inset figure depicts the magnified view in the region 440–750 nm. **e** UV–Vis absorption (top) and absorption difference (bottom) spectra of an Ar-saturated THF 1.1 mM **4′** and a 0.10 M tetrabutylammonium hexafluorophosphate supporting electrolyte recorded upon application of an anodic potential of 0.80 V vs SCE (a Pt mesh working electrode, a Pt wire counter electrode, and an Ag/$AgNO_3$ pseudo-reference electrode).

barrier compared to the other pathways, making path c the most favorable route (detailed discussion follows in the next paragraph). The resulting intermediate, **[M–H]**$^+$, can subsequently undergo deprotonation to form the net dehydrogenated product **[M–2H]**, with a total free energy change of −9.6 kcal mol^{-1}. In comparison, an alternative pathway involving hydrogen atom addition by **Host**$^{\bullet+}$ (path d) is kinetically disfavored, with a higher reaction barrier of 53.1 kcal mol^{-1}. Moreover, the intermediate formed (**MH**$^+$) does not account for the experimentally observed byproduct, which shows a red-shifted absorption profile.

We evaluated the energy profiles of paths **a**–**c**, as illustrated in Fig. 6, to identify the primary route responsible for degradation and gain insight into the kinetic aspects. The process begins with the intramolecular cyclization of **M**$^{\bullet+}$ via the transition state **A-TS**, which has an energy of 37.4 kcal mol^{-1}, leading to the formation of intermediate **B** at 31.8 kcal mol^{-1}. This cyclization step, essential for activating the C–H bonds for subsequent reactions, involves a radical addition of the oxidized azaborine unit ("core ring") to the adjacent neutral phenyl group ("pendant ring"). As a result, the positive charge is retained on the core, while the spin density shifts to the pendant ring. In intermediate **B**, the bridgehead C–H bond on the positively charged core becomes more acidic and is activated for deprotonation (path a), while the bridgehead C–H bond on the pendant ring, bearing radical character, is activated toward hydrogen atom abstraction (path b). In path a, the deprotonation by **Host** proceeds via **C′-TS1** at 46.4 kcal mol^{-1}, leading to the radical intermediate **[M–H]**$^{\bullet}$ at 40.4 kcal mol^{-1}. In path b, hydrogen atom transfer (HAT) occurs through **C′-TS2** at 54.4 kcal mol^{-1}, producing the cationic intermediate **[M–H]**$^+$ at 33.0 kcal mol^{-1}.

The most favorable pathway, however, arises when **B** reacts with **Host**$^{\bullet+}$, forming adduct **C**. In this case, hydrogen atom abstraction proceeds through **C-TS** at a much lower energy of 26.2 kcal mol^{-1}, resulting in closed-shell intermediates **[M–H]**$^+$ and **[HostH]**$^+$ at −4.6 kcal mol^{-1}. The highly exergonic nature of this step, combined with a negligible barrier of 2.4 kcal mol^{-1}, suggests that the coupling of two radicals via HAT is highly favorable and effectively irreversible. Subsequent deprotonation by **Host** from adduct **E** occurs through **E-TS** at 4.8 kcal mol^{-1} (with a step barrier of 8.7 kcal mol^{-1}) forming intermediate **F**. The overall reaction yields the final dehydrogenated product **[M–2H]** with a reaction energy of −9.6 kcal mol^{-1}. Therefore, we propose path c as the major degradation pathway, with the rate-determining step being the initial intramolecular cyclization.

While host molecules were used as reaction partners to simulate device-like environments, the energy profile for the proposed mechanism involving an oxidized dopant ($\mathbf{M}^{\bullet+}$) as a reaction partner, instead of $\mathbf{Host}^{\bullet+}$, shows a similar energetic landscape (see Supplementary Fig. 14). This confirms that the proposed mechanism remains valid under bulk electrolysis conditions as well.

Based on our mechanistic understanding, the cyclization barrier ($\Delta G^{\ddagger}_{cyc}$, the energy at **A-TS**) is identified as the key factor influencing the intrinsic stability of dopants against oxidative degradation. As shown in Table 3, the $\Delta G^{\ddagger}_{cyc}$ values calculated for dopants **1**–**4** follow the trend: **1** (38.6 kcal mol^{-1}) > **2** (37.2 kcal mol^{-1}) > **3** (36.6 kcal mol^{-1}) > **4** (35.0 kcal mol^{-1}), which explains the trend in observed Faradaic yield and device stability. The energy of the cyclized intermediate **B** (ΔG_{cyc}) follows a similar trend, except for dopant **2** having a higher ΔG_{cyc} (34.3 kcal mol^{-1}) than **1** (31.5 kcal mol^{-1}). The cyclization step, essentially a radical addition of the oxidized core, is enhanced with a more localized radical character on the reacting carbon. This is reflected in the Mulliken spin densities, which show increasing localization as **2** < **1** ~ **3** < **4** (see Supplementary Fig. 15). The distribution of the SOMO supports this, with dopant **2** displaying the most extensive π-conjugation across two fused cores and dopant **4** exhibiting the least. Additionally, the diarylamino group in dopant **3** appears to stabilize the positive charge on the core during cyclization, reducing the barrier by 2.7 kcal mol^{-1} compared to dopant **1**.

The alignment of the trends in cyclization barriers $\Delta G^{\ddagger}_{cyc}$ and stability is further supported by numerical analysis, which shows a stronger dependence of the amount of the cyclized intermediate ($[\mathbf{M}-\mathbf{H}]^{+}$) on $\Delta G^{\ddagger}_{cyc}$, rather than on the amount of $\mathbf{M}^{\bullet+}$ (see Supplementary Method 3 and Supplementary Fig. 16). This result implies that during device operation, the generation of byproducts is dominated by the intrinsic reactivity of dopants (represented by $\Delta G^{\ddagger}_{cyc}$). This finding highlights the importance of controlling $\Delta G^{\ddagger}_{cyc}$ during the molecular design stage to develop new dopants that can better resist degradation.

Finally, we investigated the deleterious effect of the degradation byproduct on the operational stability of devices. The photoluminescence spectrum of compound **4′** shows a minor bathochromic shift of 30 nm compared to that of **4**, as depicted in Supplementary Fig. 17. Contrary to initial assumptions, the robust emission from compound **4′** disputes the notion that it would impair device performance by quenching excitons or acting as a nonradiative charge carrier recombination center. This is further supported by the unaltered electroluminescence spectra between pristine devices and those operated up to the LT_{80} and LT_{50} benchmarks for compounds **1**–**4**, represented in Supplementary Fig. 18. Such consistency in emission profiles suggests that the luminescent pathways of compound **4′** do not contribute to device deterioration. However, a notable gradual decrease in current density was observed over operational time, indicating poor current performance in devices incorporating compounds

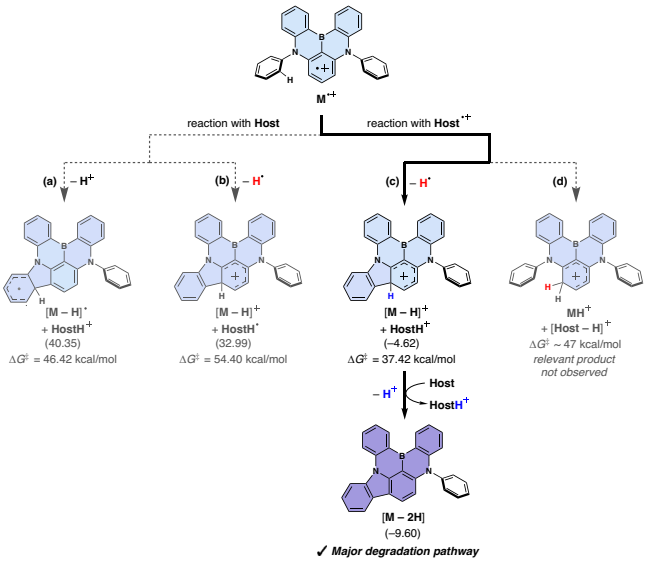

Fig. 5 | Mechanistic scenarios for oxidative degradation. Oxidative degradation pathways considered for the model MR-TADF dopant (**M**) and the truncated host molecule (**Host**).

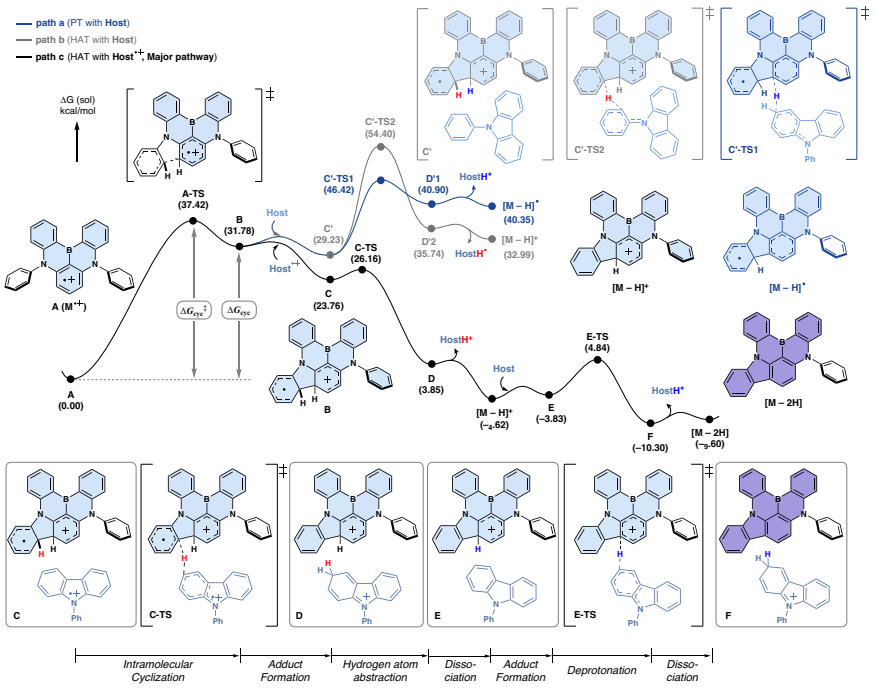

Fig. 6 | Degradation mechanism. Energy profiles were calculated for the degradation reactions (paths **a**–**c**) of the model structure of oxidized MR-TADF dopants ($\mathbf{M}^{\bullet+}$) with the truncated host molecule (**Host**). Path **c** is identified as the major degradation route.

Table 3 | Energy components of the cyclization step of MR-TADF dopants 1–4[a]

Energy (kcal mol^{-1})	1	2	3	4
$\Delta G^{\ddagger}_{cyc}$	38.56	37.19	36.61	35.00
ΔG_{cyc}	31.50	34.29	30.09	27.57

[a]Energies calculated at B3LYP-D3/Def2-TZVP//B3LYP-D3/Def2-SVP level of theory.

1–**4** when assessed at their respective LT_{80} and LT_{50} durations (Supplementary Fig. 19). This decline in current levels correspondingly led to diminished luminance, power efficiency, and EQE, as detailed in Supplementary Table 2 and Figs. 20–22. These findings collectively hint at the formation of charge carrier traps within the cyclized byproducts of MR-TADF dopants, a theory further supported by the steady increase in operational voltage over time (Supplementary Fig. 23). In fact, **4′** has the HOMO shallower than that of **4**, supporting this notion (Supplementary Fig. 4). Although we are cautious to draw direct proportionalities, we find rough correlations between the voltage rise and the LT_{95} values and the Faradaic yield values (Supplementary Fig. 24).

Deuteration effect

Deuteration has recently been demonstrated to be a viable strategy for improving the operational stability of hosts[48–51], and phosphorescent[52–55] and dipolar TADF emitters[56,57]. However, the specific mechanism by which deuterium confers protective benefits to OLED materials has not been fully elucidated. We investigated the effect of deuteration on enhancing the stability of our MR-TADF dopants. According to our proposed mechanism, wherein the rate-determining step is intramolecular cyclization, only a secondary effect is expected, as this process does not directly involve the breaking or formation of C–H bonds.

To test this hypothesis and validate our proposed mechanism, we compared the intrinsic stability of a deuterated version of compound **1**, denoted as **1D**, with its protiated form, utilizing oxidative bulk electrolysis techniques. Compound **1**, chosen for its superior polaronic stability as indicated by its Faradaic yield, served as a model for this investigation. Synthetic procedures, as well as photophysical and electrochemical data, are summarized in the "Methods" section and Supplementary Fig. 25, respectively. Our results unambiguously demonstrate the enhanced longevity of **1D**, with its oxidative degradation Faradaic yield being 30%, ~7% lower than that of compound **1** (Fig. 7a and b). This finding aligns with our quantum chemical calculations, reinforcing the premise that intermolecular hydrogen atom abstraction constitutes the secondary degradation pathway.

Further comparative studies were conducted on multilayer OLEDs fabricated with the identical configuration as used previously, substituting **1** with **1D**. The key electroluminescence data are compiled in Supplementary Table 3. Unsurprisingly, the electroluminescence spectrum and the current density versus voltage profiles of the device incorporating **1D** closely mirrored those of the device based on compound **1**. Notably, a modest increase in the EQE was observed for the **1D**-based device (24.0%) compared to the **1**-based device (23.1%) at a current density of 0.01 mA cm^{-2}, while their roll-off profiles remained virtually identical (Fig. 7e). Moreover, the operational lifetime experienced a modest improvement with the inclusion of **1D**, with the LT_{95} reaching approximately 4.3 h, an increase of about 20% over the LT_{95} of the device based on compound **1** (Fig. 7f). This improvement is greater than the error range of the LT data (±0.1%), validating the fidelity of it. This moderate increase in LT_{95} is consistent with our proposed mechanism, where the cyclization barrier is the rate-determining factor. Our calculations show a minimal vibrational correction in $\Delta G^{\ddagger}_{cyc}$ of 0.06 kcal mol^{-1}, from **1** to **1D**, resulting in a kinetic isotope effect (KIE) of 1.1. This minor KIE value further supports that the rate-determining cyclization step is responsible for the moderate increase in LT_{95}.

Discussion

Organic molecules that exhibit MR-TADF have become vital to the development of highly efficient OLEDs with saturated color purity. Despite their significance, research that closely examines the relationship between the operational lifetimes of OLEDs and the intrinsic stability of MR-TADF compounds is notably rare, even though the device's longevity is crucial for commercial viability. In our study, we discovered that the operational lifetime of OLEDs is not directly linked to the excitonic stability of MR-TADF molecules **1**–**4**. Instead, our investigations, particularly through bulk electrolysis experiments, highlighted the pronounced instability of the one-electron oxidized forms of these molecules. We established a clear correlation between the Faradaic yield for oxidative degradation and the operational lifetime of the devices, identifying radical cations—or positive polarons—as the critical intermediates that dictate device longevity.

Quantum chemical calculations propose dehydrogenative cyclization as the primary degradation pathway for the oxidized dopants, with the rate-determining step being the initial intramolecular cyclization. The cyclization occurs through the addition of the oxidized azaborine core unit to the pendant aryl group, followed by irreversible hydrogen atom abstraction and deprotonation. Analysis among dopants **1**–**4** revealed that spin localization through π-conjugation reduces reactivity toward cyclization, enhancing resistance to oxidative degradation. Chemical analyses, encompassing mass spectrometry, ^{1}H NMR spectroscopy, and UV–Vis spectro-electrochemical measurements, confirmed the formation of a cyclized byproduct following hole trapping in the MR-TADF compounds. This conclusion was further supported by our independent synthesis of the cyclization byproduct (compound **4′**).

Investigation of the deuterated MR-TADF compound **1D** demonstrated a moderate effect in reducing the Faradaic yield and extending the operational lifetime compared to its undeuterated counterpart. This modest effect is consistent with a secondary kinetic isotope effect, aligning with the proposed mechanism in which the rate-limiting step involves a transformation of C–C bond rather than C–H bond. Our findings suggest an alternative strategy for enhancing the stability of MR-TADF molecules for OLED applications, such as introducing sterically demanding substituents to inhibit the cyclization step.

This research underscores the importance of managing electrochemical reactivity to ensure the high stability of MR-TADF molecules. Given the extensive body of existing research on the electrochemical behaviors of arylamine-based organic molecules[58], we anticipate that the insights gained from our study, combined with existing knowledge, will pave the way for the design and development of highly stable MR-TADF molecules for electroluminescence applications.

Methods

General procedures

Chemicals were purchased from commercial suppliers, and used without further purification. ^{1}H and ^{13}C{^{1}H} NMR spectra were recorded on a Bruker AVANCE III HD 500 spectrometer and a Bruker AVANCE III 600 spectrometer, with CD_2Cl_2 as the solvent. Chemical shifts were referenced to the peaks corresponding to residual solvents. We examined the purity and mass spectra of materials by performing liquid chromatography-mass spectrometer-ion trap-time of flight (LCMS-IT-TOF) analyses. The LCMS-IT-TOF instrumentation consisted of a Shimadzu LC-30A Nexera SR System instrument connected to a hybrid IT-TOF mass spectrometer equipped with an ESI source. Compound **2** was prepared following the method of Kondo et al.[12]. Compound **4** was prepared following the method of Han et al.[39]. Organic

https://doi.org/10.1038/s41467-024-55620-0

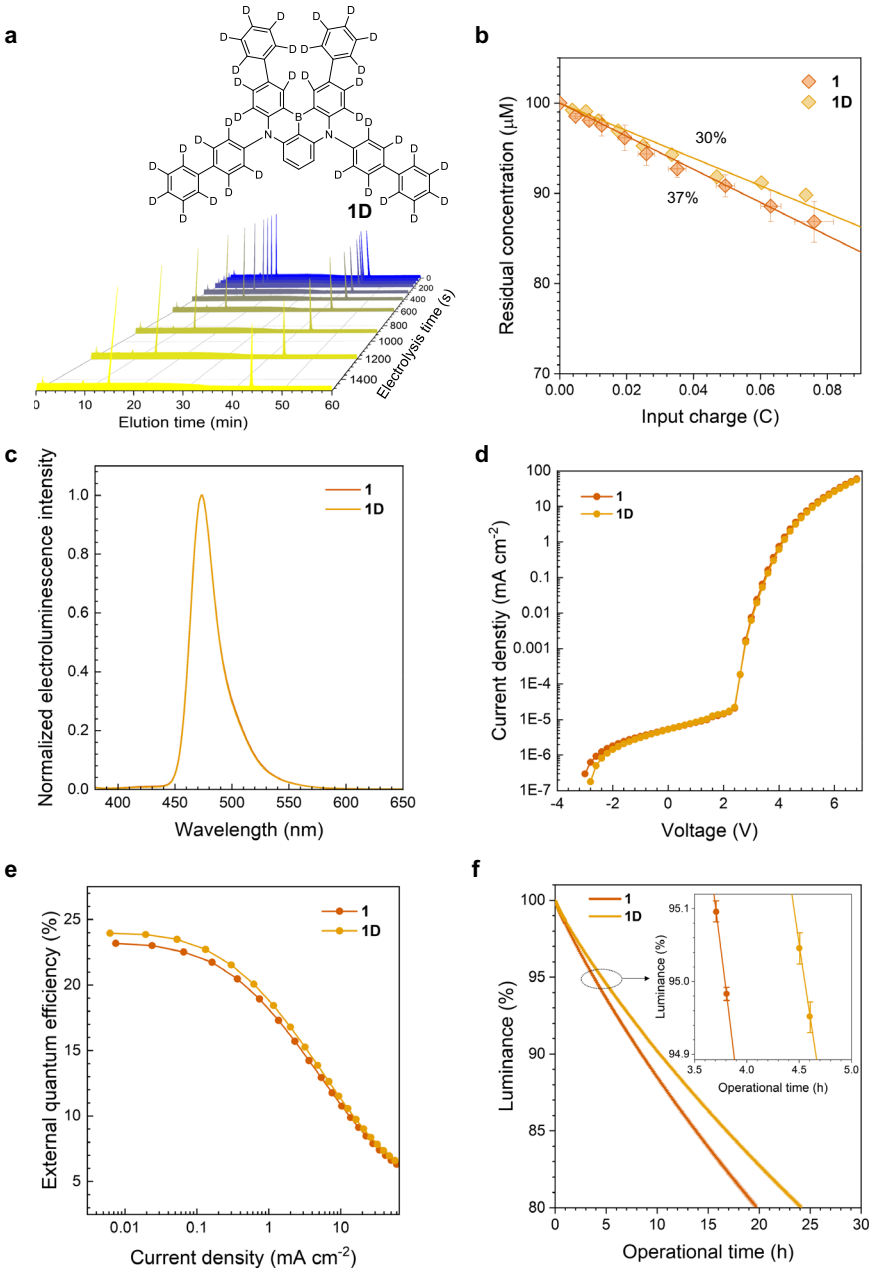

Fig. 7 | Deuteration effect. a Liquid chromatograms of 100 μM **1D** (Ar-saturated THF containing 0.10 M tetrabutylammonium hexafluorophosphate) obtained during oxidative bulk electrolysis at an anodic potential of 1.04 V vs SCE. A Pt mesh and a Pt coil were used for the working and the counter electrodes, respectively. An $Ag/AgNO_3$ pseudo reference electrode was used. The peak marked with an asterisk (*) corresponds to a benzophenone internal standard. **b** Decay in concentrations of **1** and **1D** during the continuous oxidative bulk electrolysis. The solid lines are linear fits of the data. The values are Faradaic yields for oxidative degradation of **1** and **1D**. **c**–**f** Electroluminescence spectra (**c**), current density–voltage curves (**d**), external quantum efficiencies as a function of current density (**e**), and percent luminance decays as a function of operation time of devices of **1** and **1D** driven at a constant current density at an initial luminance of 1000 cd m^{-2} (**f**). The inset figure in **f** shows a magnified view in the percent luminance range 94.9–95.1%. The luminance and power efficiency as functions of current density are shown in Supplementary Fig. 26. Error bars represent the standard deviation of three independent experiments.

materials for device fabrication were purchased from commercial suppliers and were purified by sublimation at 10^{-5} torr prior to deposition. PMMA (Mw ~120,000, Sigma–Aldrich) films doped with the MR-TADF dopants (2 wt%) were dissolved in 1,2-dichoroethane (5 wt% total solute relative to solution). The solution was sonicated for 30 min and passed through a membrane filter (pore size = 8.0 μm). An aliquot of the polymer solution was placed on a pre-cleaned glass substrate and was spin-cast using an EPLEX, SPIN-1200D spin coater. Spectrophotometric-grade THF stored under an inert atmosphere was used for spectroscopic and electrochemical measurements.

Synthesis of 1

A *tert*-butyllithium solution (1.7 M in pentane, 8.50 mL, 14.5 mmol) was added dropwise to a stirred solution of N^1,N^1,N^3,N^3-tetra([1,1′-biphenyl]-4-yl)-2-chlorobenzene-1,3-diamine (5.19 g, 6.90 mmol) in *tert*-butylbenzene (70 mL) at 0 °C under a N_2 atmosphere. The resulting mixture was heated to 60 °C and stirred for an hour. The solution was cooled to −78 °C, and boron tribromide (1.40 mL, 14.5 mmol) was slowly added. The resultant mixture was stirred for 2 h at 0 °C. After additional stirring, diisopropylethylamine (2.40 mL, 13.8 mmol) was added to the reaction mixture at 0 °C, and then the reaction mixture was heated to

110 °C and stirred for 3 h. The resultant mixture was cooled to 0 °C and then carefully quenched with saturated aq. $NaHCO_3$ solution. Extraction was performed with dichloromethane; the collected organic layer was dried over $MgSO_4$, filtered, and concentrated in vacuo. The crude mixture was purified by column chromatography on silica gel. The obtained product was recrystallized from dichloromethane/hexane/methanol to give **1** as a yellow solid (2.24 g, 45%). ^{1}H NMR (500 MHz, CD_2Cl_2): δ 9.39 (d, J = 2.0 Hz, 2H), 7.97 (d, J = 8.5 Hz, 4H), 7.84 (d, J = 8.0 Hz, 4H), 7.77 (d, J = 8.0 Hz, 6H), 7.48–7.55 (m, 12H), 7.44 (t, J = 8.0 Hz, 2H), 7.36 (t, J = 7.5 Hz, 2H), 7.34 (t, J = 8.5 Hz, 1H), 7.00 (d, J = 9.0 Hz, 2H), 6.32 (d, J = 8.0 Hz, 2H). ^{13}C{^{1}H} NMR (125 MHz, CD_2Cl_2): δ 147.16, 146.83, 141.62, 141.29, 141.16, 140.13, 133.32, 132.37, 132.22, 130.73, 129.80, 128.91, 127.83, 127.20, 126.77, 126.73, 117.75, 105.60. MS (ESI): m/z calculated for $C_{54}H_{38}BN_2$ $[M+H]^+$: 725.312, Found: 725.302.

Synthesis of 3

The full synthetic details are described in Supplementary Method 1. A *tert*-butyllithium solution (1.7 M in pentane, 8.50 mL, 14.5 mmol) was added dropsie to a stirred solution of N^5-([1,1′-biphenyl]-2-yl)-N^1,N^1,N^3,N^3,N^5-penta([1,1′-biphenyl]-4-yl)-2-chlorobenzene-1,3,5-triamine (6.19 g, 5.78 mmol) in *tert*-butylbenzene (100 mL) at 0 °C under an N_2 atmosphere. The resultant mixture was heated to 60 °C and stirred for 2 h. The solution was then cooled to −78 °C, and boron tribromide (1.40 mL, 14.5 mmol) was slowly added. The resultant mixture was stirred for an hour at 0 °C. After additional stirring, diisopropylethylamine (2.50 mL, 14.3 mmol) was added to the reaction mixture at 0 °C, then the reaction mixture was heated to 110 °C and stirred for 3 h before being cooled to 0 °C and carefully quenched with saturated aq. $NaHCO_3$ solution. The crude product was then extracted with dichloromethane, and the collected organic layer was dried over $MgSO_4$, filtered, and concentrated in vacuo. The crude mixture was purified by column chromatography on silica gel. Then the obtained product was suspended in ethyl acetate. The suspension was heated to 80 °C and stirred for an hour. The insoluble solid was collected by filtration to give **3** as a yellow solid (1.8 g, 30%). ^{1}H NMR (600 MHz, CD_2Cl_2): δ 9.33 (d, J = 2.4 Hz, 2H), 7.82 (d, J = 8.4 Hz, 4H), 7.75 (d, J = 8.4 Hz, 4H), 7.71 (dd, J = 9.0 Hz, 2.4 Hz, 2H), 7.56 (d, J = 6.6 Hz, 4H), 7.50 (t, J = 8.0 Hz, 4H), 7.33–7.42 (m, 11H), 7.27–7.31 (m, 5H), 7.21–7.24 (m, 1H), 7.14–7.16 (m, 4H), 7.11–7.14 (m, 1H), 7.04–7.08 (m, 4H), 6.99 (dd, J = 7.8 Hz, 2H), 6.97 (d, J = 8.4 Hz, 2H), 6.79 (d, J = 8.4 Hz, 2H), 5.63 (s, 2H). MS (ESI): m/z calculated for $C_{78}H_{55}BN_3$ $[M+H]^+$: 1044.448, Found: 1044.452.

Synthesis of 1D

The full synthetic details are described in Supplementary Method 2. A *tert*-butyllithium solution (1.7 M in pentane, 5.50 mL, 9.35 mmol) was added dropwise to a stirred solution of N^1,N^1,N^3,N^3-tetrakis([1,1′-biphenyl]-4-yl-d_9)-2-chlorobenzene-1,3-diamine (3.50 g, 4.45 mmol) in *tert*-butylbenzene (90 mL) at 0 °C under an N_2 atmosphere. The resultant mixture was heated to 60 °C and stirred for an hour. The solution was cooled to −78 °C and boron tribromide (0.90 mL, 9.34 mmol) was slowly added. The resultant mixture was stirred for 2 h at 0 °C. After additional stirring, diisopropylethylamine (1.60 mL, 9.15 mmol) was added to the reaction mixture at 0 °C; the mixture was then heated to 110 °C and stirred for 3 h. The resultant mixture was cooled to 0 °C and carefully quenched with saturated aq. $NaHCO_3$ solution. The crude product was then extracted with dichloromethane, and the collected organic layer was dried over $MgSO_4$, filtered, and concentrated in vacuo. The crude mixture was purified by column chromatography on silica gel. Then the obtained product was recrystallized from dichloromethane/hexane/methanol to give **1D** as a yellow solid (0.800 g, 24%). ^{1}H NMR (500 MHz, CD_2Cl_2): δ 7.98 (s, 0.17H), 7.84 (s, 2.1H), 7.78 (s, 2.3H), 7.51–7.55 (m, 1H), 7.44 (s, 0.3H), 7.37 (s, 0.28H), 7.35 (t, J = 8.5 Hz, 1H), 6.99 (s, 0.4H), 6.32 (d, J = 8.5 Hz, 2H); deuterium is incorporated at ~80%. ^{13}C{^{1}H} NMR (125 MHz, CD_2Cl_2): δ 147.11, 146.84, 141.17, 132.21, 127.07, 126.62, 105.56. MS (ESI): m/z calculated for $C_{54}H_{10}D_{27}BN_2$ $[M\text{-}7D+7H]^+$: 751.474, Found: 751.387.

Device fabrication and characterization

The organic layers were deposited consecutively onto pre-cleaned ITO glass substrates using a thermal evaporation system at a pressure less than 1.0×10^{-6} torr. A 1 nm-thick LiQ layer and a 100 nm-thick Al layer were deposited as a cathode via thermal evaporation. The deposition rates of the organic and metal layers were 0.1 and 0.5 nm s^{-1}, respectively. LiQ was deposited at a rate of 0.01 nm s^{-1}. The active device area of 4 mm^2 was defined by the area of overlap between the ITO and Al electrodes. The current, voltage, and luminance of the OLED devices were measured with a system comprising a Keithley 2400 SourceMeter and a Topcon SR-3AR spectroradiometer. Operational lifetime measurements of the devices were conducted in a constant-current mode. Current–voltage characteristics of single-carrier devices with the device structure introduced in Supplementary Fig. 10 were measured with a system consisting of a Keithley 2400 source-meter. On the basis of the lack of emission under the given voltage, we inferred that only hole transport occurred within the single-carrier devices.

Steady-state UV–Vis absorption measurements

UV–Vis absorption spectra were collected at 298 K using an Agilent Cary 300 spectrophotometer. Stock solutions with a concentration of 10 mM were prepared in THF. Sample solutions with a concentration of 10 μM in THF, which had been previously saturated with Ar, were prepared prior to the measurements by diluting the stock solution unless otherwise stated. A total of 3.0 mL of each solution was added to a quartz cell (Hellma, beam path length = 1.0 cm).

Steady-state photoluminescence measurements

Photoluminescence spectra were obtained at 298 K by using a Photon Technology International Quanta Master 400 scanning spectrofluorometer. Samples for the measurements were prepared as 10 μM solutions in THF, unless otherwise stated. The solutions were deaerated by bubbling Ar gas for at least 10 min before the measurement. All operations were controlled with the FelixGX software provided by the manufacturer.

Photoluminescence lifetime measurements

PMMA films doped with (quartz substrate) 2 wt% **1**–**4** were used for the determination of the photoluminescence lifetimes. Photoluminescence decay traces were acquired using time-correlated single-photon-counting techniques with a PicoQuant, FluoTime 200 instrument after picosecond pulsed laser excitation (pulse duration = 2.5 ns). A diode laser that produced 377 nm pulses (PicoQuant, LDH375) was driven by a PDL800-D driver (PicoQuant). Transient photon signals were collected at λ_{obs} = 471 nm (**1**), 467 nm (**2**), 461 nm (**3**), and 459 nm (**4**). The burst mode was used to monitor delayed fluorescence. The fluorescence signals at the emission peak wavelengths of the compounds were obtained with an automated motorized monochromator. Photoluminescence decay profiles were analyzed (OriginPro 8.0, OriginLab) using a biexponential decay model. Temperature-dependent measurements were conducted in the temperature range 79–315 K using an Oxford Instruments Omicron Nanoscience, Optistat DN2 variable-temperature liquid N_2 cryostat equipped with a MercuryiTC temperature controller.

Electrochemical characterization

Cyclic and differential pulse voltammetry experiments were conducted using a CH Instruments CHI630 B potentiostat in conjunction with a three-electrode cell assembly. A Pt wire and a glassy carbon disc were used as the counter and working electrodes, respectively. An Ag/$AgNO_3$ couple was used as the pseudo-reference electrode. Measurements were carried out in Ar-saturated THF (2.0 mL) with 0.10 M

tetrabutylammonium hexafluorophosphate as the supporting electrolyte at scan rates of 100 mV s^{-1} (cyclic voltammetry) and 4.0 mV s^{-1} (differential pulse voltammetry). The ferrocenium/ferrocene couple was used as an external reference.

Spectroelectrochemical measurements

UV–Vis absorption spectra of the radical species were acquired via the amperometric *I*–*t* curve method using an Agilent Cary 300 spectrophotometer with anodic potentials applied. A blank spectrum was acquired for a 0.10 M tetrabutylammonium hexafluorophosphate solution (THF) in a spectroelectrochemical cell (path length = 0.5 mm) equipped with a Pt mesh working electrode, a Pt wire counter electrode, and an $Ag/AgNO_3$ pseudo-reference electrode. A 1.0 mM sample solution (500 μL) was delivered into the spectroelectrochemical cell for the measurement.

Photolysis

An Ar-saturated 25 mL THF solution containing 100 μM sample was placed in a 40 mL scintillation vial equipped with a Teflon-coated magnetic stir bar. The solution was photoirradiated using a monochromatic light source (450 nm) positioned 1 cm from the vial. Aliquots of the 100 μL reaction mixture were collected during the photolysis reaction and diluted with 50 μL of 1.0 mM of benzophenone in THF and 850 μL CH_3CN for quantification of the residual concentration of the components. High-performance liquid chromatography (HPLC) experiments were performed on an Agilent 6120 DW LC/MSD instrument equipped with a Poroshell, EC-C18 column. The photolyzed solutions, diluted in HPLC grade CH_3CN (1:4, v/v), were passed through a poly(vinylidene fluoride) (PVDF) membrane filter (pore size = 8.0 μm) prior to injection. A 5 μL sample volume was injected and allowed to pass through the column at room temperature; a gradient eluent with increasing fractions of CH_3CN in H_2O was used. The quantum yields for photolysis (Φ_{deg}) were determined according to Eq. (1):

$$\Phi_{deg} = \frac{k_{obs} \times V}{(1 - 10^{-Abs}) \times q} \tag{1}$$

where k_{obs} represent the degradation rate corresponding to the slope of the linear fit of the initial five data points shown in Supplementary Fig. 6b, *V* is the volume of the solution (25 mL), $1–10^{-Abs}$ is the photokinetic factor based on the absorbance at a wavelength of 450 nm, and *q* is the photon flux (4.0×10^{-8} einstein s^{-1}) determined using standard ferrioxalate actinometry and additionally confirmed using an optical powermeter.

Oxidative bulk electrolysis

Oxidative bulk electrolysis experiments were conducted using 25 mL of Ar-saturated THF solutions containing 200 μM sample, along with 0.10 M tetrabutylammonium hexafluorophosphate, in a 40 mL scintillation vial equipped with a Teflon-coated magnetic stir bar. Oxidative bulk electrolysis was performed at potentials of 1.04 V vs SCE for **1** and **3**, 1.01 V vs SCE for **2**, and 0.98 V vs. SCE for **4**. A Pt mesh and a Pt coil served as the working and counter electrodes, respectively. An $Ag/AgNO_3$ pseudo-reference electrode was used. Changes in the Faradaic charge transferred from the working electrode during oxidative bulk electrolysis were monitored. Aliquots of the 100 μL reaction mixture were collected during the electrolysis reaction and diluted with 50 μL of 1.0 mM benzophenone in THF and 850 μL CH_3CN for quantification of the residual concentration of the components. HPLC experiments were performed on an Agilent 6120 DW LC/MSD instrument equipped with a Poroshell, EC-C18 column. The electrolyzed solutions, diluted in HPLC grade CH_3CN (1:4, v/v), were passed through a PVDF membrane filter (pore size = 8.0 μm) prior to injection. A 5 μL sample volume was injected and allowed to pass through the column at room temperature; a gradient eluent with increasing fractions of CH_3CN in H_2O was used. The Faradaic yield for oxidative bulk electrolysis was determined following Eq. (2):

$$\text{Faradaic yield} = \frac{k_{obs} \times V \times t}{C \times F} \tag{2}$$

where k_{obs} is the degradation rate corresponding to the slope of the linear fit of the initial five data points shown in Fig. 3b, *V* is the volume of the solution (25 mL), *t* is the reaction time, *C* is the total charge transferred at time *t*, and *F* is the Faraday constant.

Degradation product analyses

ESI mass analyses were performed under positive-ion detection mode (voltage = 70 V) in the range 200–1500 amu.

Determination of rate constants for ISC and rISC

The (r)ISC rate constants were analyzed based on Eqs. (3)–(6) developed by Ying et al.[59]:

$$k_r^{S1} = \Phi_{PF} k_{PF} + \Phi_{DF} k_{DF} \tag{3}$$

$$k_{nr}^{S1} = \frac{1 - \Phi_{total}}{\Phi_{total}} k_r^{S1} \tag{4}$$

$$k_{rISC} \approx \frac{(\Phi_{PF} + \Phi_{DF}) k_{PF} k_{DF}}{\Phi_{PF} k_{PF} + \Phi_{DF} k_{DF}} = \frac{\Phi_{total} k_{PF} k_{DF}}{k_r^{S1}} \tag{5}$$

$$k_{ISC} = \frac{\Phi_{PF} \Phi_{DF} k_{PF} k_{DF} (k_{PF} - k_{DF})^2}{(\Phi_{PF} k_{PF} + \Phi_{DF} k_{DF})^2 k_{rISC}} \approx \frac{\Phi_{PF} \Phi_{DF} (k_{PF} - k_{DF})^2}{k_r^{S1} \Phi_{total}} \tag{6}$$

In these equations, k_{nr}^{S1} is the nonradiative decay rate of the S_1 state, k_{PF} is the rate for prompt fluorescence, k_{DF} is the rate for delayed fluorescence, k_{ISC} is the rate for intersystem crossing from the S_1 state to the T_1 state, k_{rISC} is the rate for reverse intersystem crossing, Φ_{PF} is the quantum yield for prompt fluorescence, Φ_{DF} is the quantum yield for delayed fluorescence, and $\Phi_{total} = \Phi_{PF} + \Phi_{DF}$.

Quantum chemical calculation methods

All density functional theory (DFT)[58] calculations were performed with the Orca 4.2.0 suite of quantum chemistry programs[59]. Geometries of intermediates and transition states were optimized with B3LYP[60,61] hybrid functional along with Grimme's D3 dispersion[62] correction (B3LYP-D3) using the Ahlrichs balanced basis sets of split valence quality, Def2-SVP[63]. The RIJCOSX approximation[64,65] was employed to accelerate Coulomb integrals using the Def2/J auxiliary basis set[66]. Single point calculations were carried out with the valence polarized triple-zeta (ζ) quality Ahlrichs basis set, Def2-TZVP[63], to obtain more reliable electronic energies of the optimized structures. To evaluate the zero-point energy (ZPE) and entropy correction, the frequency calculations were performed at the same level of theory used in the geometry optimization. In order to simulate the dielectric shielding effect within the emission layer in our OLED device, the dielectric constant of the HT host molecule, which is the major component of the emissive layer, was evaluated using Clausius–Mossotti relation[67], as follows:

$$\frac{\varepsilon - 1}{\varepsilon + 2} = \frac{4\pi\alpha}{3V} \tag{7}$$

where α is the isotropic component of the molecular polarizability and *V* is the volume occupied by a single molecule. The polarizability was calculated as 70.3 $Å^3$, and the volume was obtained as 510 $Å^3$ using

Multiwfn software[68]. Thus, the dielectric constant $\varepsilon = 5.101$ was obtained for the thin-film environment composed of HT host. Using the epsilon value, the solvation energies were calculated based on the conductor-like polarizable continuum model[69] on the gas-phase optimized structures, to consider the shielding effect. The solution-phase Gibbs free energies were computed as follows:

$$G(\mathrm{sol}) = G(\mathrm{gas}) + G\mathrm{solv} \tag{8}$$

$$G(\mathrm{gas}) = H(\mathrm{gas}) - TS(\mathrm{gas}) \tag{9}$$

$$H(\mathrm{gas}) = E(\mathrm{SCF}) + \mathrm{ZPE} \tag{10}$$

$$\Delta G(\mathrm{sol}) = \Sigma G(\mathrm{sol})\text{for products} - \Sigma G(\mathrm{sol})\text{for reactants} \tag{11}$$

G(sol) is the solvation-corrected Gibbs free energy from gas phase free energy G(gas); H(gas) is the enthalpy in the gas phase; T is the temperature (298.15 K); S(gas) is the entropy in the gas phase; E(SCF) is the self-consistent field converged electronic energy; and ZPE is the vibrational zero-point energy. Note that entropy here refers specifically to the vibrational/rotational/translational entropy of the solute(s). The solvent entropies are implicitly included in the continuum model[60–62].

Data availability

The datasets generated during and/or analyzed during the current study are available from the corresponding author on request. The raw data for the main figures generated in this study are provided as excel spreadsheet in the Source Data file.

Code availability

The code used for the numerical analysis is based on ode solver built in SciPy and regression analysis built in Sklearn code using a python package. The python code data and detailed methods are provided in the Supplementary Information/Source Data file.

References

1. Baldo, M. A., Lamansky, S., Burrows, P. E., Thompson, M. E. & Forrest, S. R. Very high-efficiency green organic light-emitting devices based on electrophosphorescence. *Appl. Phys. Lett.* **75**, 4–6 (1999).
2. Lamansky, S. et al. Synthesis and characterization of phosphorescent cyclometalated iridium complexes. *Inorg. Chem.* **40**, 1704–1711 (2001).
3. Lamansky, S. et al. Highly phosphorescent bis-cyclometalated iridium complexes: synthesis, photophysical characterization, and use in organic light emitting diodes. *J. Am. Chem. Soc.* **123**, 4304–4312 (2001).
4. Holmes, R. J. et al. Blue organic electrophosphorescence using exothermic host–guest energy transfer. *Appl. Phys. Lett.* **82**, 2422–2424 (2003).
5. Longhi, E. & De Cola, L. in *Iridium (III) in Optoelectronic and Photonics Applications* (ed Eli Zysman-Colman) 205–274 (John Wiley & Sons Ltd., 2017).
6. Baldo, M. A. et al. Highly efficient phosphorescent emission from organic electroluminescent devices. *Nature* **395**, 151–154 (1998).
7. Fleetham, T., Li, G., Wen, L. & Li, J. Efficient "pure" blue OLEDs employing tetradentate Pt complexes with a narrow spectral bandwidth. *Adv. Mater.* **26**, 7116–7121 (2014).
8. Uoyama, H., Goushi, K., Shizu, K., Nomura, H. & Adachi, C. Highly efficient organic light-emitting diodes from delayed fluorescence. *Nature* **492**, 234–238 (2012).
9. Liu, Y., Li, C., Ren, Z., Yan, S. & Bryce, M. R. All-organic thermally activated delayed fluorescence materials for organic light-emitting diodes. *Nat. Rev. Mater.* **3**, 18020 (2018).
10. Hamze, R. et al. Eliminating nonradiative decay in Cu(I) emitters: >99% quantum efficiency and microsecond lifetime. *Science* **363**, 601–606 (2019).
11. Hatakeyama, T. et al. Ultrapure blue thermally activated delayed fluorescence molecules: efficient HOMO–LUMO separation by the multiple resonance effect. *Adv. Mater.* **28**, 2777–2781 (2016).
12. Kondo, Y. et al. Narrowband deep-blue organic light-emitting diode featuring an organoboron-based emitter. *Nat. Photonics* **13**, 678–682 (2019).
13. Pershin, A. et al. Highly emissive excitons with reduced exchange energy in thermally activated delayed fluorescent molecules. *Nat. Commun.* **10**, 597 (2019).
14. Naveen, K. R., Palanisamy, P., Chae, M. Y. & Kwon, J. H. Multi-resonant TADF materials: triggering the reverse intersystem crossing to alleviate the efficiency roll-off in OLEDs. *Chem. Commun.* **59**, 3685–3702 (2023).
15. Suresh, S. M., Hall, D., Beljonne, D., Olivier, Y. & Zysman-Colman, E. Multiresonant thermally activated delayed fluorescence emitters based on heteroatom-doped nanographenes: recent advances and prospects for organic light-emitting diodes. *Adv. Funct. Mater.* **30**, 1908677 (2020).
16. Ha, J. M., Hur, S. H., Pathak, A., Jeong, J.-E. & Woo, H. Y. Recent advances in organic luminescent materials with narrowband emission. *NPG Asia Mater.* **13**, 53 (2021).
17. Monkman, A. Why do we still need a stable long lifetime deep blue OLED emitter? *ACS Appl. Mater. Interfaces* **14**, 20463–20467 (2022).
18. Kim, H. J. & Yasuda, T. Narrowband emissive thermally activated delayed fluorescence materials. *Adv. Opt. Mater.* **10**, 2201714 (2022).
19. Fan, X. et al. RGB thermally activated delayed fluorescence emitters for organic light-emitting diodes toward realizing the BT.2020 standard. *Adv. Sci.* **10**, 2303504 (2023).
20. Baldo, M. A., Adachi, C. & Forrest, S. R. Transient analysis of organic electrophosphorescence. II. Transient analysis of triplet-triplet annihilation. *Phys. Rev. B* **62**, 10967–10977 (2000).
21. Meerheim, R. et al. Influence of charge balance and exciton distribution on efficiency and lifetime of phosphorescent organic light-emitting devices. *J. Appl. Phys.* **104**, 014510 (2008).
22. Jurow, M. J., Bossi, A., Djurovich, P. I. & Thompson, M. E. In situ observation of degradation by ligand substitution in small-molecule phosphorescent organic light-emitting diodes. *Chem. Mater.* **26**, 6578–6584 (2014).
23. Bangsund, J. S., Hershey, K. W. & Holmes, R. J. Isolating degradation mechanisms in mixed emissive layer organic light-emitting devices. *ACS Appl. Mater. Interfaces* **10**, 5693–5699 (2018).
24. Giebink, N. C. et al. Intrinsic luminance loss in phosphorescent small-molecule organic light emitting devices due to bimolecular annihilation reactions. *J. Appl. Phys.* **103**, 044509 (2008).
25. Siboni, H. Z., Luo, Y. & Aziz, H. Luminescence degradation in phosphorescent organic light-emitting devices by hole space charges. *J. Appl. Phys.* **109**, 044501 (2011).
26. Liu, S., Peng, C., Cruz, A., Chen, Y. & So, F. Degradation study of organic light-emitting diodes with solution-processed small molecule phosphorescent emitting layers. *J. Mater. Chem. C* **4**, 8696–8703 (2016).
27. Schmidt, T. D., Jäger, L., Noguchi, Y., Ishii, H. & Brütting, W. Analyzing degradation effects of organic light-emitting diodes via transient optical and electrical measurements. *J. Appl. Phys.* **117**, 215502 (2015).
28. Kim, S. et al. Degradation of blue-phosphorescent organic light-emitting devices involves exciton-induced generation of polaron pair within emitting layers. *Nat. Commun.* **9**, 1211 (2018).

29. Moon, Y. K. et al. Modeling electron-transfer degradation of organic light-emitting devices. *Adv. Mater.* **33**, 2003832 (2021).
30. Zhao, C., Li, C., Li, Y., Qiu, Y. & Duan, L. Understanding the operational lifetime expansion methods of thermally activated delayed fluorescence sensitized OLEDs: a combined study of charge trapping and exciton dynamics. *Mater. Chem. Front.* **3**, 1181–1191 (2019).
31. Meng, Q.-Y. et al. Longevity gene responsible for robust blue organic materials employing thermally activated delayed fluorescence. *Nat. Commun.* **14**, 3927 (2023).
32. van der Zee, B., Li, Y., Wetzelaer, G.-J. A. H. & Blom, P. W. M. Triplet-polaron-annihilation-induced degradation of organic light-emitting diodes based on thermally activated delayed fluorescence. *Phys. Rev. Appl.* **18**, 064002 (2022).
33. So, F. & Kondakov, D. Degradation mechanisms in small-molecule and polymer organic light-emitting diodes. *Adv. Mater.* **22**, 3762–3777 (2010).
34. Scholz, S., Kondakov, D., Luessem, B. & Leo, K. Degradation mechanisms and reactions in organic light-emitting devices. *Chem. Rev.* **115**, 8449–8503 (2015).
35. Lee, Y.-T. et al. Tailor-made multi-resonance terminal emitters toward narrowband, high-efficiency, and stable hyperfluorescence organic light-emitting diodes. *Adv. Optical Mater.* **10**, 2200682 (2022).
36. Meng, G. et al. Highly efficient and stable deep-blue OLEDs based on narrowband emitters featuring an orthogonal spiro-configured indolo[3,2,1-*de*]acridine structure. *Chem. Sci.* **13**, 5622–5630 (2022).
37. Xue, W. et al. Identifying the molecular origins of green BN-TADF material degradation and device stability via in situ Raman spectroscopy. *Chem. Eur. J.* **28**, e202201006 (2022).
38. Wang, X., Wang, L., Meng, G., Zeng, X., Zhang, D. & Duan, L. Improving the stability and color purity of a BT.2020 blue multi-resonance emitter by alleviating hydrogen repulsion. *Sci. Adv.* **9**, eadh1434 (2023).
39. Han, S. H., Jeong, J. H., Yoo, J. W. & Lee, J. Y. Ideal blue thermally activated delayed fluorescence emission assisted by a thermally activated delayed fluorescence assistant dopant through a fast reverse intersystem crossing mediated cascade energy transfer process. *J. Mater. Chem. C* **7**, 3082–3089 (2019).
40. Giebink, N. C., D'Andrade, B. W., Weaver, M. S., Brown, J. J. & Forrest, S. R. Direct evidence for degradation of polaron excited states in organic light emitting diodes. *J. Appl. Phys.* **105**, 124514 (2009).
41. Wetzelaer, G. A. H., Kuik, M., Nicolai, H. T. & Blom, P. W. M. Trap-assisted and Langevin-type recombination in organic light-emitting diodes. *Phys. Rev. B* **83**, 165204 (2011).
42. Nebauer, J. et al. Oxidative cyclodehydrogenation of trinaphthylamine: selective formation of a nitrogen-centered polycyclic π-system comprising 5- and 7-membered rings. *Angew. Chem. Int. Ed.* **61**, e202205287 (2022).
43. Jones, A. W., Louillat-Habermeyer, M.-L. & Patureau, F. W. Strained dehydrogenative ring closure of phenylcarbazoles. *Adv. Synth. Catal.* **357**, 945–949 (2015).
44. Ambrose, J. F. & Nelson, R. F. Anodic oxidation pathways of carbazoles: I. carbazole and N-substituted derivatives. *J. Electrochem. Soc.* **115**, 1159 (1968).
45. Fukushima, T. et al. Material degradation of liquid organic semiconductors analyzed by nuclear magnetic resonance spectroscopy. *AIP Adv.* **5**, 087124 (2015).
46. Prachumrak, N. et al. Synthesis and characterization of carbazole dendronized coumarin derivatives as solution-processed non-doped emitters and hole-transporters for electroluminescent devices. *New J. Chem.* **38**, 3282–3294 (2014).
47. Zhang, D., Cai, M., Zhang, Y., Zhang, D. & Duan, L. Sterically shielded blue thermally activated delayed fluorescence emitters with improved efficiency and stability. *Mater. Horiz.* **2**, 145–151 (2016).
48. Kondakov, D. Y., Brown, C. T., Pawlik, T. D. & Jarikov, V. V. Chemical reactivity of aromatic hydrocarbons and operational degradation of organic light-emitting diodes. *J. Appl. Phys.* **107**, 024507 (2010).
49. Liu, X. et al. Isotope effect of host material on device stability of thermally activated delayed fluorescence organic light-emitting diodes. *Small Sci.* **1**, 2000057 (2021).
50. Tsuji, H., Mitsui, C. & Nakamura, E. The hydrogen/deuterium isotope effect of the host material on the lifetime of organic light-emitting diodes. *Chem. Commun.* **50**, 14870–14872 (2014).
51. Yao, J., Dong, S.-C., Tam, B. S. T. & Tang, C. W. Lifetime enhancement and degradation study of blue OLEDs using deuterated materials. *ACS Appl. Mater. Interfaces* **15**, 7255–7262 (2023).
52. Abe, T., Miyazawa, A., Konno, H. & Kawanishi, Y. Deuteration isotope effect on nonradiative transition of *fac*-tris (2-phenylpyridinato) iridium (III) complexes. *Chem. Phys. Lett.* **491**, 199–202 (2010).
53. Wang, P. et al. Synthesis of all-deuterated tris(2-phenylpyridine)iridium for highly stable electrophosphorescence: the "deuterium effect. *J. Mater. Chem. C* **1**, 4821–4825 (2013).
54. Bae, H. J. et al. Protecting benzylic C-H bonds by deuteration doubles the operational lifetime of deep-blue Ir-phenylimidazole dopants in phosphorescent OLEDs. *Adv. Optical Mater.* **9**, 2100630 (2021).
55. Li, W. et al. Improved efficiency and stability of red phosphorescent organic light-emitting diodes via selective deuteration. *J. Phys. Chem. Lett.* **13**, 1494–1499 (2022).
56. Jung, S. et al. Enhancing operational stability of OLEDs based on subatomic modified thermally activated delayed fluorescence compounds. *Nat. Commun.* **14**, 6481 (2023).
57. Huang, T. et al. Enhancing the efficiency and stability of blue thermally activated delayed fluorescence emitters by perdeuteration. *Nat. Photonics* **18**, 516–523 (2024).
58. Karon, K. & Lapkowski, M. Carbazole electrochemistry: a short review. *J. Solid State Electrochem.* **19**, 2601–2610 (2015).
59. Ying, A. et al. High-efficiency red electroluminescence based on a carbene–Cu(I)–acridine complex. *ACS Appl. Mater. Interfaces* **13**, 13478–13486 (2021).
60. Nayak, P. K. & Periasamy, N. Calculation of ionization potential of amorphous organic thin-films using solvation model and DFT. *J. Org. Chem.* **10**, 532–535 (2009).
61. Lu, T. & Chen, F. Multiwfn: a multifunctional wavefunction analyzer. *J. Comp. Chem.* **33**, 580–592 (2012).
62. Barone, V. & Cossi, M. Quantum calculation of molecular energies and energy gradients in solution by a conductor solvent model. *J. Phys. Chem. A* **102**, 1995–2001 (1998).
63. Weigend, F. & Ahlrichs, R. Balanced basis sets of split valence, triple zeta valence and quadruple zeta valence quality for H to Rn: design and assessment of accuracy. *Phys. Chem. Chem. Phys.* **7**, 3297–3305 (2005).
64. Neese, F. An improvement of the resolution of the identity approximation for the formation of the Coulomb matrix. *J. Comput. Chem.* **24**, 1740–1747 (2003).
65. Wennmohs, F., Hansen, A. & Becker, U. Efficient, approximate and parallel Hartree–Fock and hybrid DFT Calculations. A "chain-of-Spheres" algorithm for the Hartree–Fock exchange. *Chem. Phys.* **356**, 98–109 (2009).
66. Weigend, F. Accurate Coulomb-fitting basis sets for H to Rn. *Phys. Chem. Chem. Phys.* **8**, 1057–1065 (2006).
67. Nayak, P. K. & Periasamy, N. Calculation of Ionization potential of amorphous organic thin-films using solvation model and DFT. *Org. Electron.* **10**, 532–535 (2009).
68. Lu, T. & Chen, F. Multiwfn: a multifunctional wavefunction analyzer. *J. Comput. Chem.* **33**, 580–592 (2012).
69. Barone, V. & Cossi, M. Quantum calculation of molecular energies and energy gradients in solution by a conductor solvent model. *J. Phys. Chem. A* **102**, 1995–2001 (1998).

Acknowledgements
We gratefully acknowledge Dmitry Androsov, Ju Hyun Kim, Sangmo Kim, Eunkyung Lee, and Yusuke Maruyama for their contributions to the preparation of the materials used in this study. This work was supported by the Midcareer Research Program (RS–2023-00208856 to Y.Y.) through National Research Foundation grants funded by the Ministry of Science, Information, and Communication Technology (ICT) and Future Planning (MSIP), and by the Institute for Basic Science in Korea (IBS-R010-A1 to M.-H.B.).

Author contributions
B.H.J. performed the spectroscopic experiments, analyzed the data, and wrote the manuscript. H.S.K. synthesized and characterized the materials, and co-wrote the manuscript. J.H.B. performed oxidative bulk electrolysis. J.K. fabricated and tested the devices. Y.P., E.L., H.M., and C.O. conducted and analyzed the quantum chemical calculations and Y.P. co-wrote the manuscript. Y.J. coordinated the material preparation and OLED experiments. S.C. performed the electrochemical experiments. M.-H.B. supervised the quantum chemical calculations at KAIST and co-wrote the manuscript. Y.Y. coordinated all of the experiments and analyses and co-wrote the manuscript. All authors contributed to the discussion of the study and edited the manuscript.

Competing interests
The authors declare no competing interests.

Additional information
Supplementary information The online version contains supplementary material available at https://doi.org/10.1038/s41467-024-55620-0.

Correspondence and requests for materials should be addressed to Yongsik Jung, Mu-Hyun Baik or Youngmin You.

Peer review information *Nature Communications* thanks the anonymous, reviewer(s) for their contribution to the peer review of this work. A peer review file is available.